

Enhanced Photoelectrochemical Properties of Fe-TiO₂ Nanotube Films: A Combined Experimental and Theoretical Study

Yanfeng Zhu

Department of Chemical Engineering and Safety, Binzhou University, Binzhou, Shandong 256603, PR China

E-mail: yanfengzhu2014@163.com

Received: 25 February 2021 / Accepted: 15 April 2021 / Published: 30 April 2021

Fe-doped TiO₂ nanotube array (Fe-TiO₂ TNTA) films are produced by a simple and facile anodization method on Ti foil substrates. The Fe-doped TNTA films were characterized by SEM, Raman, XPS and UV-vis spectrum. The result showed that the absorption edge generated bathochromic shift. Raman and XPS reveal that Ti⁴⁺ ions were uniformly substituted by Fe³⁺ ions or Ti-O-Fe bonds. After comparing different Fe³⁺ ions concentrations, 0.1M Fe-doped TiO₂ samples exhibit the highest photocurrent value, indicating super photoelectrochemical activity. The difference between the photocathodic protection properties of TNTA films and Fe-doped TNTA films is also investigated. The density functional theory (DFT) calculation is carried out to confirm the effects of the Fe³⁺ ions on the absorption edge redshift and the bandgap changes.

Keywords: TiO₂ nanotube arrays; Fe-doped; Photoelectrochemical; EIS; DFT calculations;

1. INTRODUCTION

In 1999, Zwillig and co-workers first reported the milestone work of the feasibility to fabricate the TiO₂ nanotube arrays film on Ti sheet by anodic oxidation[1]. Thereafter, a variety of different TiO₂ nanotubes have been fabricated in F⁻ contained electrolytes of H₃PO₄, H₂SO₄, H₃BO₃, Na₂SO₄, ethylene glycol and glycerol[2-6]. Over the past few decades, TiO₂ nanotubes have been vastly studied in many areas, such as photocatalysts, hydrogen production, solar cells and gas sensors[7-10]. However, the extremely high recombination of photo-carriers and large bandgap ($E_g = 3.2$ eV) for pure TiO₂ limit the use for solar irradiation driven applications[11]. Intense efforts have been taken to accelerate the photoelectric conversion properties of TiO₂ nanotubes[12-15].

Transitional metal ions doping can effectively improve the photoelectric converting performance of TiO₂ nanomaterials[16-18]. Doping can tune the intrinsic properties of TiO₂, which can in turn improve the photoelectric conversion performance.

Fe ion doping to TiO₂ nanomaterials has received significant attention. It is well-known that the radiuses of Fe³⁺ and Ti⁴⁺ ions are similar, giving rise to the Fe³⁺ ion inserting into the crystal structure or replacing a Ti atom in the Ti-O-Ti network to form a Ti-O-Fe bond [19, 20]. Several studies suggest that Fe³⁺ ions could serve as shallow charge traps, and enlarge the TiO₂ photoabsorption edge into the visible region. However, there is a significant divergence in the role of Fe³⁺ cations. Some researchers have argued that Fe³⁺ ions could narrow the bandgap of TiO₂, while others have claimed that Fe³⁺ ions could generate a new electronic state in the bandgap. Thus, in order to understand the function of Fe³⁺ on photoelectrochemical performance of TiO₂, experimental verification and the density functional theory (DFT) calculation are combined to carry out this research.

In this paper, the Fe-doped TiO₂ NTA film was achieved by the anodization technique. The influence of Fe³⁺ ions dopant on the photoelectrochemical properties has also been investigated. DFT calculation was used to interpret experimental results and to clarify the fundamental structure of the Fe-doped TiO₂ NTA sample.

2. EXPERIMENTAL SECTION

2.1. Material

All the chemical reagents in this work were of analytical grade and used as received without further purification. Ethanol, acetone, HF, H₃PO₄, Fe(NO₃)₃, Na₂SO₄, KCl, NaCl were obtained from Sinopharm Chemical Reagent Co., Ltd. Ti foil (99.7% purity) and 304 stainless steel (SS) were purchased from Tianjin Yuanhao metal materials Co. LTD.

2.2 Fabrication of Fe-doped TNTA films

Ti foils (15 mm × 10 mm × 0.1 mm) were successively cleaned by sonication in acetone, ethanol, and distilled water. Subsequently, the pretreatment Ti foils were anodized in 0.5 wt.% HF or 0.5 wt.% HF + 1.0 mol·L⁻¹ H₃PO₄ electrolyte solution containing different concentrations Fe(NO₃)₃ aqueous solution (0.05, 0.1, 0.15 M) under 20 V for 30 min. The Fe-doped TiO₂ NTA samples were labeled according to the Fe content: TiFe 0.05, TiFe 0.1, TiFe 0.15. For comparative experiments, the undoped TiO₂ NTA sample was fabricated by anodic oxidation on the surface of Ti foils under 20 V in 0.5 wt.% HF or 0.5 wt.% HF + 1.0 mol·L⁻¹ H₃PO₄ electrolyte solution for 30 min, labeled as TiFe 0_[HF] and TiFe 0_[HF+H₃PO₄], respectively. After the anodization, the samples were rinsed with water. Finally, the as-prepared samples were calcined at 450 °C for 2 h at a heating rate of 5 °C min⁻¹, subsequently cooled down to room temperature.

2.3 Characterization.

The samples' morphologies were observed with the scanning electron microscope (SEM, Hitachi, S4800). A UV-vis spectrophotometer (Varian, Cary 5000) was used to measure the

photoabsorption properties of samples. The X-ray photoelectron spectroscopy (XPS) measurements were accomplished on a PHI Quantum 2000 system with Al K α as an exciting X-ray source. The binding energies were determined by the C 1s electrons at 284.4 eV. In addition, the Raman spectra of the films were achieved at room temperature by using a Renishaw UV-vis Raman microscope system.

2.4 Photoelectrochemical measurements.

The photocurrent measurement was carried out in a 0.4 M Na₂SO₄ solution under illumination of the Xe lamp. The nanotube array films, Pt wire, and saturated calomel electrode (SCE) were served as the working electrode (WE), counter electrode (CE), and reference electrode (RE), respectively. The photocathodic protection effect of the photoanodes were carried out by a composite system including a photoelectrochemical cell and a corrosion cell. A salt bridge was used to connect the two cells. The 304 stainless steel (304SS) to be protected was coupled to the photoanode by a copper wire. The photocathodic protection properties of the photoanode were studied by the electrode potential test and electrochemical impedance spectroscopy (EIS) measurement.

2.5 Computational models and details

All of the calculations were carried out using the DMol³ code based on the Material Studio software package. The electron exchange correlation effects and electron-ion interactions were treated with the Perdew-Burke-Ernzerhof generalized gradient approximation (PBE-GGA)[21], combined with the all-electron double numerical quality (DNP) basis set including polarization functions.

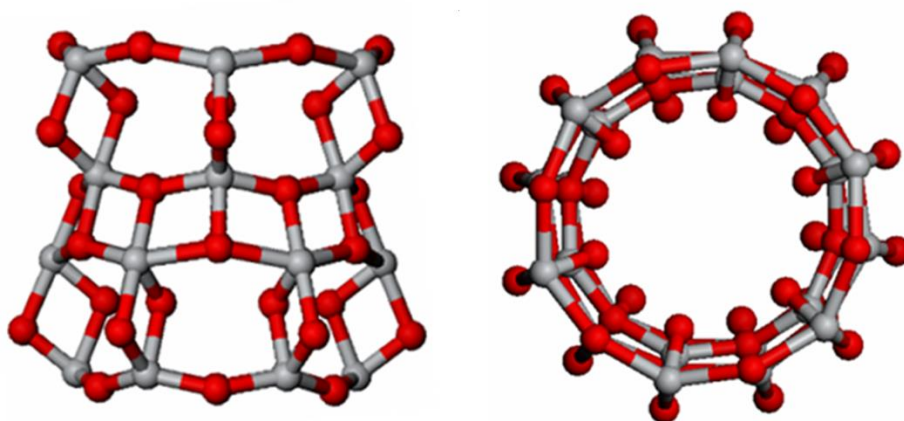


Figure 1. Optimized geometry of a TiO₂ nanotube (12,0) segment with the minimum repeated unit. The side and top view of the TiO₂ nanotube are presented in the left and right panels, respectively. The O atoms are displayed in red, while Ti atoms are presented in gray.

Effective core potentials (ECP) were commonly used to account for some or all of the core electrons of heavy atoms[22, 23]. The TiO₂ (101) surfaces were modeled by vacuum slabs[24, 25]. Figure 1 demonstrates the optimized geometrical configuration of a single-walled TiO₂ nanotube (12, 0) segment. A rectangular supercell with a size of 4 nm×4 nm × *c* nm was built for a TiO₂ nanotube, and

the length of c equal to the periodicity of TiO_2 nanotubes. The k -points grid was set to $1 \times 1 \times 5$. The energetic convergence threshold for the self-consistent field (SCF) is $1.0 \times 10^{-5} \text{ eV atom}^{-1}$.

Due to the similar radius of Fe^{3+} and Ti^{4+} , the model for the Fe-doped TiO_2 sample was created by substituting Ti atoms with Fe atoms in the slab of TiO_2 , corresponding to the concentration of 1.45 wt.% and 2.90 wt.% Fe. The interrelated models were shown in Figure 2.

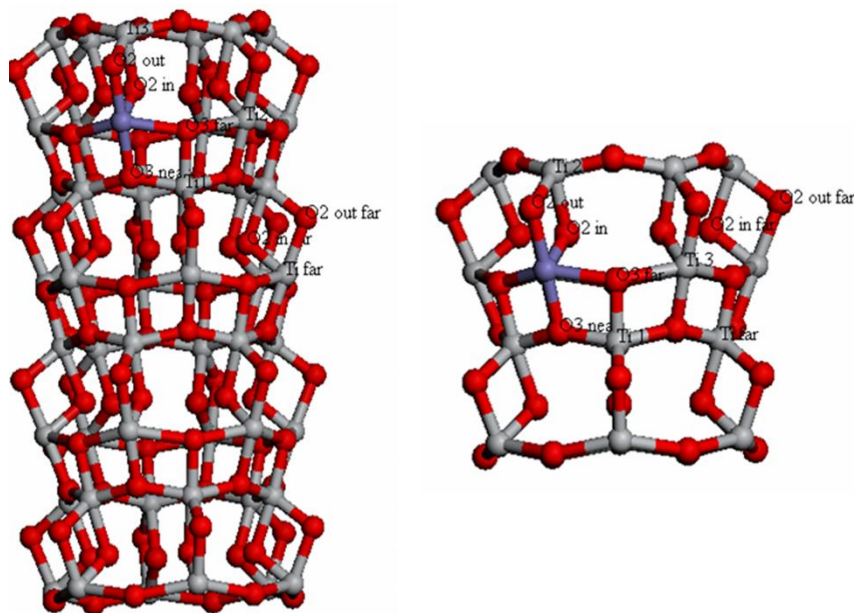


Figure 2. The models of Fe-doped TiO_2 with different Fe concentrations of (left) 1.45 wt.% and (right) 2.90 wt.%. The Ti, O and Fe atoms are displayed in gray, red and purple.

3. RESULTS AND DISCUSSION

The SEM images of the samples fabricated in different electrolytes are displayed in Figure 3. The nanotubular structures could be identified. In Figure 3a, pores with various sizes were found on the sample surface anodized in the HF electrolyte; that is, the tube diameter was uneven. In contrast, HF/ H_3PO_4 system could fabricate more uniform nanotubes during the anodization process, as shown in Figure 3c. One hypothesis is that H_3PO_4 can act as a pH buffer solution to provide a steady pH value and, regulate the equilibrium between the dissolution and the acidification during pore growth[26]. Figure 3b and Figure 3d present the SEM images of the Fe-doped TiO_2 NTA film. The surface morphology did not show a significant change comparing to the TiO_2 NTA film, only a little increase for the surface roughness.

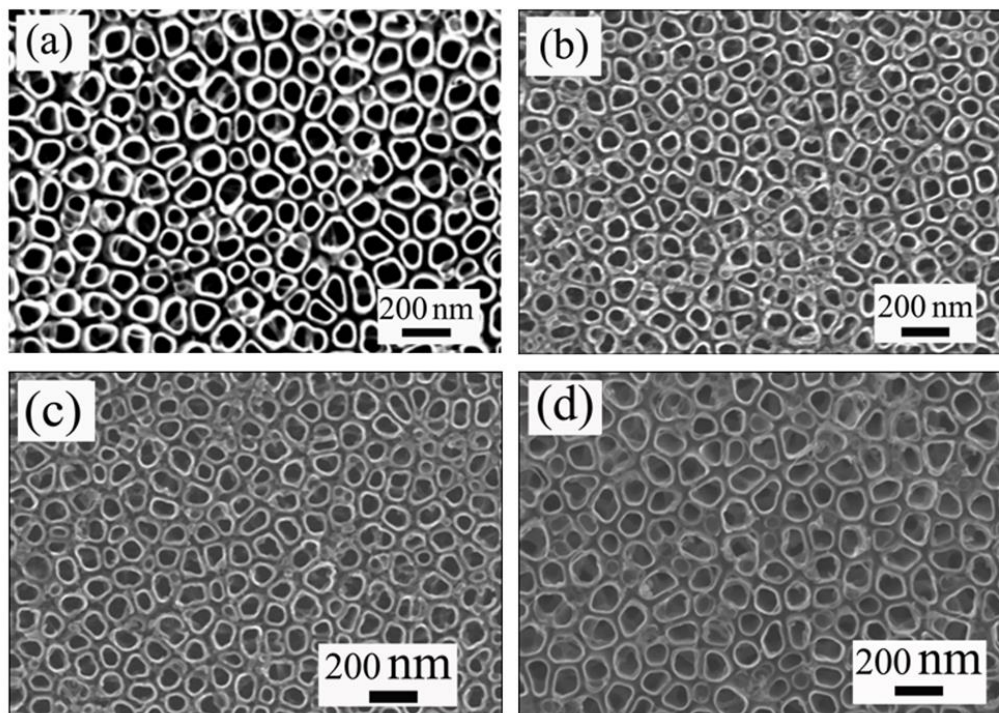


Figure 3. SEM images of the nanotube array films prepared in different solutions (a) HF, (b) HF + Fe(NO₃)₃, (c) HF + H₃PO₄, (d) HF + H₃PO₄ + Fe(NO₃)₃.

The Raman spectroscopy is a powerful technique to investigate the near-surface defect owing to its surface sensitiveness. The Raman spectra of the different films fabricated in HF+ H₃PO₄ system is shown in Figure 4. The symmetric vibration modes of the anatase phase TiO₂ were identified at 141 cm⁻¹ (*E_g*), 199 cm⁻¹ (*E_g*), 396 cm⁻¹ (*B_{1g}*), 516 cm⁻¹ (*A_{1g}*), and 636 cm⁻¹ (*E_g*)[27]. With regard to the Fe-doped TiO₂ NTA film, all the peaks corresponded to the anatase TiO₂ crystalline structure, no characteristic peaks of iron ions were observed. This indicated that Fe³⁺ ions might be identified as the displacement doping in the TiO₂ crystal lattice[28,29]. When Fe³⁺ ions occupied the Ti⁴⁺ sites, a crystal structure disordering occurred, and some new intrinsic lattice defects such as oxygen vacancies were introduced, to balance the charge states. Furthermore, the peaks are broadened and shifted towards the longer wavelength with the increase of Fe³⁺ ions content. The *E_g* (141 cm⁻¹) mode is associated with O-O interaction, thus, it is sensitive to the oxygen vacancies[30].

Figure 5 displays the XPS spectra of the different samples. From the Figure 5A, Ti, O, C, and Fe elements were observed. For the TiO₂ sample, two peaks located at 459.6 eV (Ti 2p_{3/2}) and 465.3 eV (Ti2p_{1/2}) could be confirmed, which was a criterion of Ti⁴⁺ species in the Fe-TiO₂ sample[31, 32]. Compared to the position of the Ti 2p peak in undoped TiO₂, the values of that in Fe-doped TiO₂ showed slight change. This implied that the Fe³⁺ ions had a certain impact on the Ti 2p local chemical state [33]. Since Fe³⁺ and Ti⁴⁺ ions have similar radiuses, Ti-O-Fe bonds can be formed due to Fe³⁺ entering into the TiO₂ crystal lattice [29, 34]. For the sake of maintaining charge balance, Ti⁴⁺ might turn into a high valence, which led to the Ti 2p peaks shift. The XPS spectrum of O 1s could be decomposed into two peaks. The low binding energy peak was assigned to the oxygen atoms of the TiO₂ lattice[29]. The high binding energy could be identified as the (-OH) or H₂O on the TiO₂ surface[35]. Furthermore, Figure

5C indicated that the O 1s XPS spectra of Fe-doped TiO₂ had a certain amount of shifting compared with that of TiO₂, which could be due to a change of the ionic state of the oxygen bond[36]. Figure 5D shows the XPS spectra of Fe 2p. The principal peak at a binding energy of 710.7 eV was assigned to Fe 2p_{3/2}, and the minor peak at 724.3 eV was assigned to Fe 2p_{1/2} [37]. Consequently, the Fe element might exist in the form of Fe³⁺ and Ti-O-Fe bonds in the lattices.

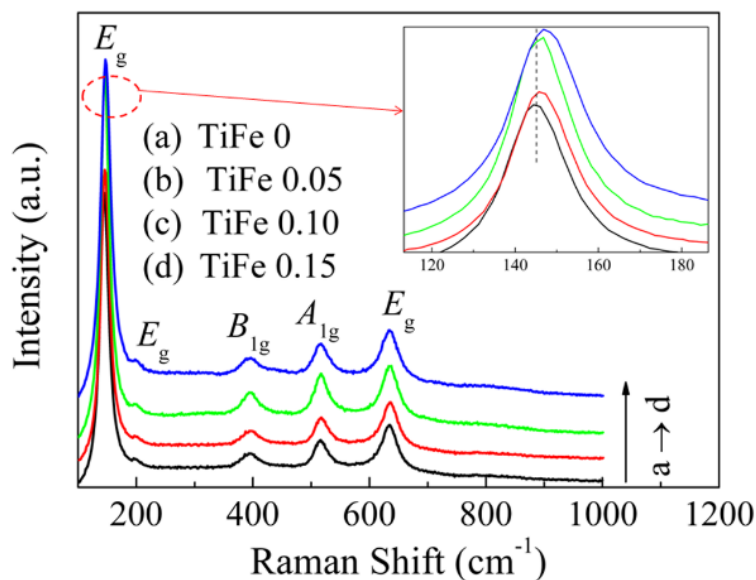


Figure 4. Raman spectra of different films.

Figure 6. reveals that the absorption edge for TiO₂ was at 387 nm, which was accordance with the E_g of anatase TiO₂ ($E_g = 3.2$ eV)[11]. Moreover, it is can be seen that the absorption curve between 340 nm and 800 nm was wavy, because of the interaction of the TiO₂ film and the Ti substrate[38]. Compared to the absorption edge in curve a, the absorption edge of curve b showed a small red shift. The result indicated that P-doped could reduce the energy band of TiO₂. When H₃PO₄ is the electrolyte, (PO₄)³⁻ entered into the TiO₂ nanotube arrays through diffusion. Then (PO₄)³⁻ might absorb on the wall of tubes, then modify the tubes surface [39]. Therefore, P-doped could play to the redshift of the absorption range of the sample. The absorption range of the Fe-doped TiO₂ film (curve c) shifted towards longer wavelengths compare with that of un-doped TiO₂ film (curve b). The red shift could be attributed to two reasons. One is that electronic states were introduced into the band-gap [40]. The other is a d-d transition of Fe³⁺ [20, 36, 41].

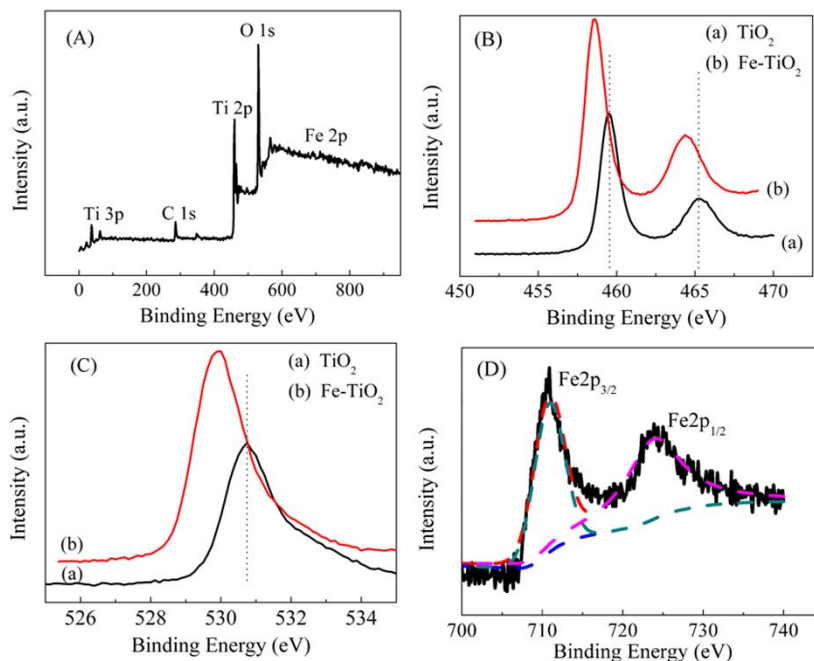


Figure 5. XPS spectra of (A) total spectrum of the Fe–TiO₂ film, (B) Ti 2p, (C) O 1s, (D) Fe.

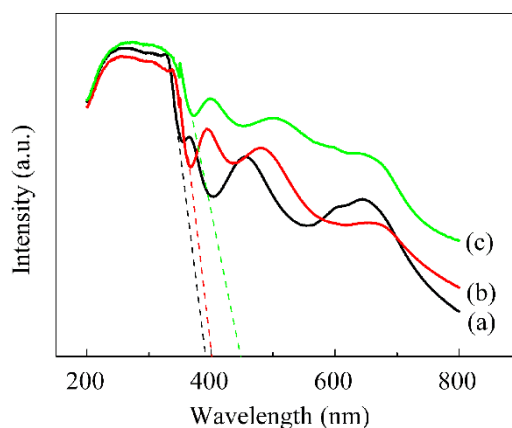


Figure 6. The UV-vis absorption spectra of films prepared in different solutions (a) HF, (b) HF + H₃PO₄, (d) HF + H₃PO₄ + Fe(NO₃)₃.

Figure 7 illustrates the photocurrent spectra of different samples. The results show that a significant photocurrent was generated for all samples under illumination. The photoanodes exhibited n-type semiconductor behavior, i.e., positive photocurrent. Moreover, the photocurrent values of samples fabricated in HF/H₃PO₄ solution were higher than that of samples prepared in HF solution. This result indicated that P-doped could improve the transfer ability of electrons in the semiconductor. Moreover, it could obviously observe that the photocurrent value of Fe-doped TiO₂ NTA samples was significantly enhanced at lower doping content. In addition, the TiFe 0.1 NTA sample exhibited the highest photocurrent value. The enhanced photocurrent of Fe-doped TiO₂ NTA samples is mainly due to the red

shift of the light absorption range and the lower recombination rate of h^+e^- pairs[42]. Furthermore, the photocurrent value of the TiFe 0.15 sample is less than that of the undoped TiO_2 sample. At higher Fe doping content, Fe ions could serve as recombination centers, as reported in some of earlier investigations[43, 44]. As a result of the higher recombination rate, the photocurrent value decreased.

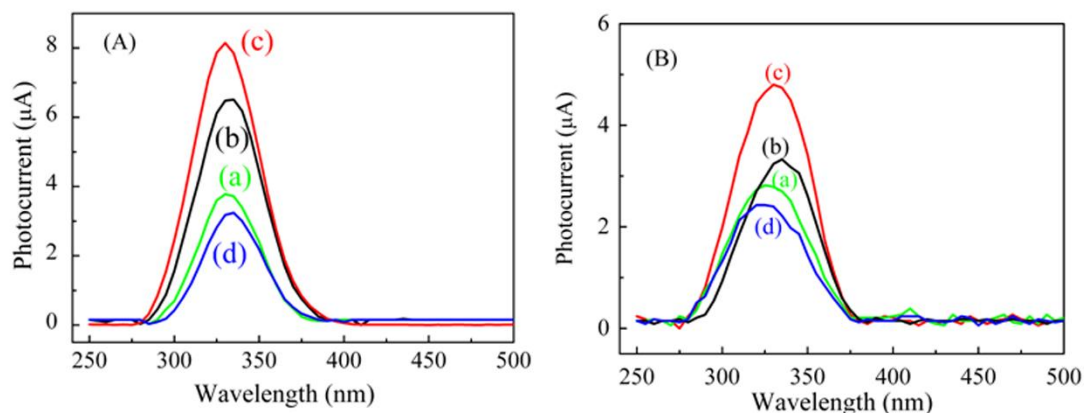
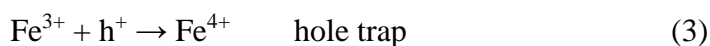
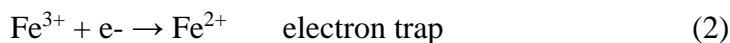
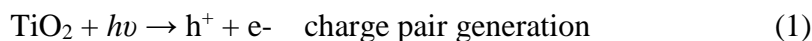
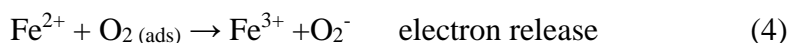


Figure 7. The photocurrent spectra of different samples prepared in different solutions (A) $HF + H_3PO_4 + Fe(NO_3)_3$, (B) $HF + Fe(NO_3)_3$. (a) TiFe 0, (b) TiFe 0.05, (c) TiFe 0.10, (d) TiFe 0.15

The role of Fe^{3+} ions may be twofold. Firstly, the absorption wavelength shifted toward long wavelength due to the ions doping. Secondly, Fe^{3+} also acted as a carrier of the hole and electron transmission at a suitable concentration. When TiO_2 is irradiated under UV light, the way of the production of photoelectrons was shown in equation (1). A moderate amount of Fe^{3+} ions served as the trap inhibit the recombination of electron-hole pairs[45, 46]. The main processes are as the equation of (2) and (3):



Based on the crystal theory, the $3d^5$ orbital of the Fe^{3+} ion is half-filled, which is a stable state. Compared to Fe^{3+} ions, Fe^{4+} or Fe^{2+} ions are in a relatively unstable state. The trapped charges released in the following reactions:



However, above an optimal concentration, Fe^{3+} ions might accelerate the recombination photogenerated carriers, owing to decreased distance between trapped sites. Consequently, the properties of photoelectric conversion decreased.

The potential-time curves of 304 SS coupled or uncoupled with different photoanode films are shown in Figure 8. The measurement was performed under light on or off conditions. The results

indicated that the electrode potential of 304 SS shifted negatively under illumination conditions, and then kept a negative value steadily. The drop of potential of the 304 SS was a consequence of the injection of photogenerated electrons from the photoanode[47, 48]. However, when the light was off, the electrode potential increased rapidly because the photoanode could no longer generate photoelectrons. From the Figure 8, it could be seen that the potential of 304SS decreased by about 400 mV and 460 mV for curve (a) and (b), respectively. In other words, the $\text{TiFe}_{[\text{HF}^+ \text{H}_3\text{PO}_4]}$ photoanode could make the potential of 304SS drop more negative than the $\text{TiFe}_{[\text{HF}]}$ photoanode. The result indicated that the $\text{TiFe}_{[\text{HF}^+ \text{H}_3\text{PO}_4]}$ photoanode might afford a better photocathodic protection performance.

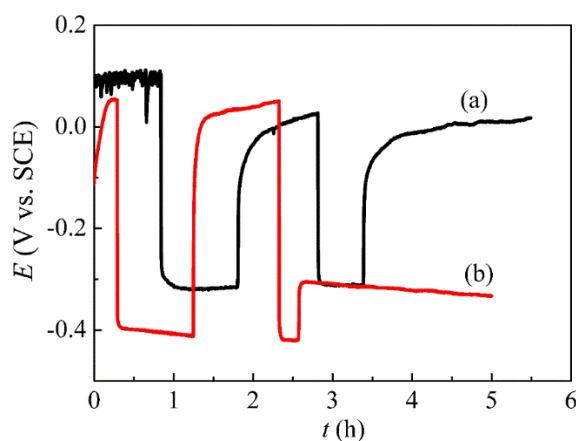


Figure 8. Time evolution of the potential of 304 stainless steel coupled to different film photoanodes under interrupted illumination. (a) $\text{TiFe}_{[\text{HF}]}$, (b) $\text{TiFe}_{[\text{HF}^+ \text{H}_3\text{PO}_4]}$

Moreover, the photocathodic protection properties were also measured using the electrochemical impedance spectroscopy (EIS), which could exhibit significant quantitative and qualitative corrosion data[49, 50]. Figure 9 displays Nyquist plots of 304SS uncoupled and coupled to photoanodes under illumination conditions. The equivalent circuit (Figure 10) was proposed as a model for fitting the EIS result. R_s , R_t and C_{dl} represent the electrolyte resistance, the charge transfer resistance and the double layer capacitance, respectively. The diameter arc of pure 304SS uncoupled to the photoanode presented a large arc (curve a), and the value of R_t was $255.6 \text{ k}\Omega \text{ cm}^2$. Under irradiation, the diameter of impedance arcs of 304SS coupled to photoanodes decreased remarkably compared with pure 304SS. The injection of photoelectrons from photoanodes to the 304SS electrode will accelerate electrochemical reaction rate at the electrode/solution interface, which can lead to the R_t values degradation. Comparing curve b with (c), the EIS shape was similar, but the diameter of curve c was smaller than that of curve (b). Hence, the level of electron transport in the $\text{TiFe}_{[\text{HF}^+ \text{H}_3\text{PO}_4]}$ film had got an obviously improvement. According to the mechanism of photocathodic protection, the more photoelectrons transferred into the protected metal, the better photocathodic protection properties could be achieved.

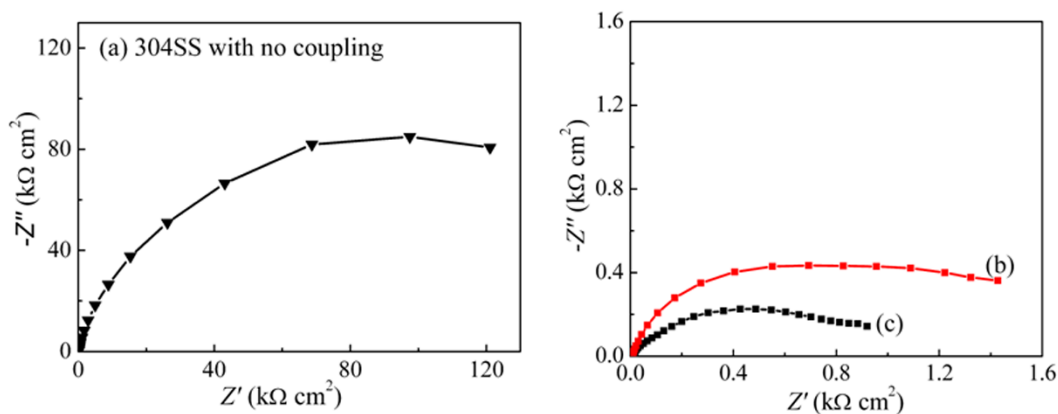


Figure 9. Nyquist plots of 304 stainless steel in a 0.5 M NaCl solution under different conditions. (a) No coupling, (b) coupled to the TiFe_[HF] photoanode (c) coupled to the TiFe_[HF+ H3PO4] photoanode.

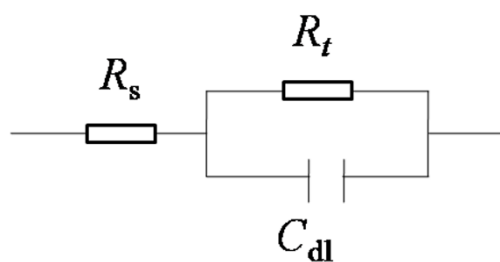


Figure 10. Simulating equivalent circuits for the EIS results.

To explain the performance of Fe doping on the band structure and the partial density of states of TiO₂, DFT calculations were performed. As shown in Figure 11, the DFT calculations indicate that the band gap was about 2.50 eV for undoped TiO₂. The value became small compare to the theoretical value (3.20 eV), that is, the scissor operation is 0.70 eV. This was mainly due to the shortcoming of exchange-correction functional in excited states or the well-known limitation of GGA arithmetic[51]. Moreover, two different impure states were above the valence band maximum (VBM) and the other was below the conduction band minimum (CBM), respectively. The calculated band gaps of 1.45 wt.% and 2.90 wt.% Fe-doped TiO₂ were 2.42 and 2.29 eV. Due to the existence of the scissor operation (0.70 eV), the corrected band gaps of 1.45 wt.% Fe-doped TiO₂ and 2.90 wt.% Fe-doped TiO₂ samples were 3.12 eV and 2.99 eV, respectively, that is, the energy gap of Fe-doped TiO₂ samples decreased remarkably. The presence of impure energy levels reduced the carriers transition energy, and the electrons can be excited step by step[52]. Consequently, the absorption edges generated bathochromic shift, which was consistent with the experimental results.

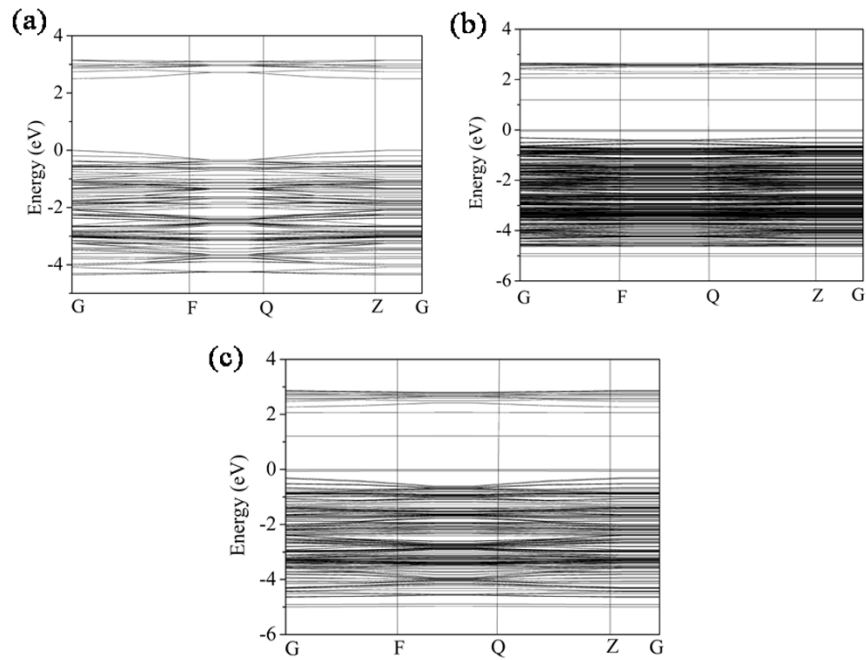


Figure 11. Band structure plots of (a) TiO_2 , (b) 1.45wt.%Fe- TiO_2 and (c) 2.90wt.%Fe- TiO_2 .

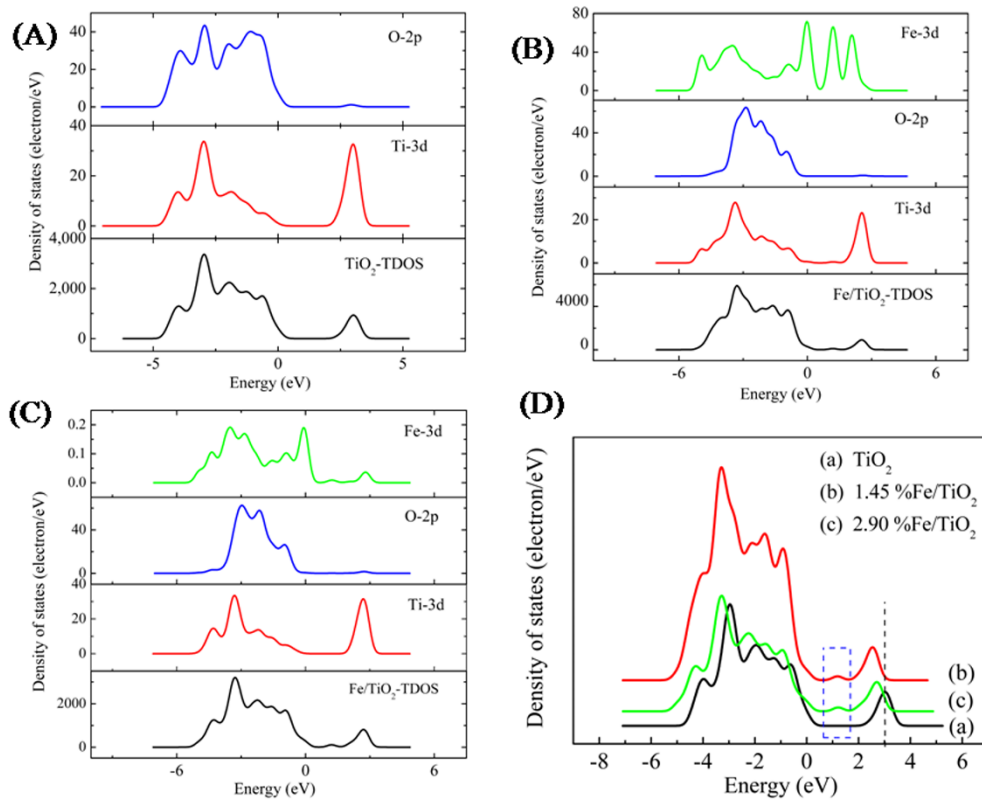


Figure 12. Total and partial density of states of (A) TiO_2 , (B) 1.45wt.%Fe- TiO_2 and (C) 2.90wt.%Fe- TiO_2 .

Figure 12 shows that the CB was mainly composed of Ti 3d orbitals for the TiO₂. The VB was composed of by O 2p and Ti 3d orbitals. For Fe-doped TiO₂, the prominent contribution to the VB is O 2p, Fe 3d and Ti 3d orbitals, and the new energy levels[53]. The hybridization effect could promote the migration of photocarriers. From Figure 12D, the bottom of CBs of Fe-doped TiO₂ decreased, which induced the redshift of the UV-vis absorption range. Consequently, the DFT results show that the Fe-doped TiO₂ sample enhanced the photoactivity compared to undoped TiO₂ samples.

4. CONCLUSIONS

We fabricated of Fe-doped TiO₂ NTA films by a simple one-step anodic oxidation technology. The results showed that and an appropriate amount of Fe ions could efficiently inhibit the recombination rate of photogenerated electron hole, and significantly improve the photoelectrochemical performance of the TiO₂ nanotubes. The electrode potential and EIS measurements suggested the film could provide a stable photocathodic protection effect on the 304SS. Combining experimental and DFT results, the cause of the enhanced photoactivity of the Fe-doped TiO₂ sample is due to the generation of new electronic states within the band-gap of TiO₂. More importantly, we believe that the application of this film can also be extended to various areas, including water splitting and photocatalysis.

ACKNOWLEDGEMENT

This work was supported by the Natural Science Foundation of Shandong Province of China (ZR2016BP11, ZR2018LE002), A Project of Shandong Province Higher Educational Science (J16LC18) and Science Research Fund of Binzhou University (2014Y19).

References

1. V. Zwillig, E. Darque-Ceretti, A. Boutry-Forveille, D. David, M. Y. Perrin, M. Aucouturier, *Surf. Interface Anal.*, 27 (1999) 629.
2. J. Yoo, K. Lee, A. Tighineanu, P. Schmuki, *Electrochem. Commun.*, 34 (2013) 177.
3. C. M. Ruan, M. Paulose, O. K. Varghese, C. A. Grimes, *Sol. Energ. Mat. Sol. C*, 90 (2006) 1283.
4. M. Balakrishnan, R. Narayanan, *Thin Solid Films*, 540 (2013) 23.
5. C. A. Grimes, M. Paulose, H. E. Prakasam, O. K. Varghese, L. Peng, K. C. Papat, G. K. Mor, T. A. Desai, *J. Phys. Chem. C*, 111 (2007) 14992.
6. D. Regonini, A. Satka, A. Jaroenworarluck, D. W. E. Allsopp, C. R. Bowen, R. Stevens, *Electrochim. Acta*, 74 (2012) 244.
7. J. Wang, H. Zhu, S. Tang, M. Li, Y. Zhang, W. Xing, Q. Xue, L. Yu, *J. Alloy. Compd.*, 842 (2020) 155869.
8. Z. Yan, W. Wang, L. Du, J. Zhu, D. L. Phillips, J. Xu, *Appl. Catal. B- Environ.*, 275 (2020) 119151.
9. J. M. Sun; X. J. Yang, L. Zhao, B. H. Dong, S. M. Wang, *Mater. Lett.*, 260 (2020) 126882.
10. A. V. Lashkov, F. S. Fedorov, M. Y. Vasilkov, A. V. Kochetkov, I. V. Belyaev, I. A. Plugin, A. S. Varezchnikov, A. N. Filipenko, S. A. Romanov, A. G. Nasibulin, G. Korotcenkov, V. V. Sysoev, *Sensor. Actuat. B-Chem.*, 306 (2020) 127615.
11. A. El Ruby Mohamed, S. Rohani, *Energ. Environ. Sci.*, 4 (2011) 1065.
12. I. Barba-Nieto, K. C. Christoforidis, M. Fernandez-Garcia, A. Kubacka, *Appl. Catal. B-Environ.*, 277 (2020) 119246.

13. H. S. Moon, K. J. Yong, *Appl. Surf. Sci.*, 530 (2020) 147215.
14. H. C. Geng, N. Jiang, C. Y. Li, X. Q. Zhu, Y. Qiao, Q. Y. Cai, *Nanotechnology*, 31 (2020) 395602.
15. X. W. Cheng, H. L. Liu, Q. H. Chen, J. J. Li; P. Wang, *J. Hazard. Mater.*, 254 (2013) 141.
16. S. Y. Li, Y. L. Yang, Q. Su, X. Y. Liu, H. P. Zhao, Z. X. Zhao, J. Li, C. Jin, *Mater. Lett.*, 252 (2019) 123.
17. M. S. Hassan, T. Amna, O. B. Yang, H. C. A. Kim, M. S. Khil, *Ceram. Int.*, 817 (2020) 5925.
18. J. L. Nie, Y. Mo, B. Z. Zheng, H. Y. Yuan, D. Xiao, *Electrochim. Acta*, 90 (2013) 589.
19. K. Melghit, O. S. Al-Shukeili, I. Al-Amri, *Ceram Int.*, 35 (2009) 433.
20. A. Eshaghi, H. Moradi, *Adv. Powder Technol.*, 29 (2018) 1879.
21. J. P. Perdew, K. Burke, M. Ernzerhof, *Phys. Rev. Lett.*, 77 (1996) 3865.
22. X. Cao, M. Dolg, *Wires Comput. Mol. Sci.*, 1 (2011) 200.
23. M. Rezaei, A. N. Chermahini, *Int. J. Hydrogen Energy*, 45 (2020) 20993.
24. H. Liu, K. Tan, *Comput. Theor. Chem.*, 991 (2012) 98.
25. V. Nagarajan, R. Chandiramouli, *Ceram. Int.*, 40 (2014) 16147.
26. J. M. Macak, H. Tsuchiya, P. Schmuki, *Angew. Chem. Int. Edit.*, 44 (2005) 2100.
27. I. A. Mkhaliid, J. L. G. Fierro, R. M. Mohamed, A. A. Alshahri, *Ceram. Int.*, 46 (2020) 25822.
28. S. D. Delekar, H. M. Yadav, S. N. Achary, S. S. Meena, S. H. Pawar, *Appl. Surf. Sci.*, 263 (2012) 536.
29. N. A. Kyeremateng, V. Hornebecq, H. Martinez, P. Knauth, T. Djenizian, *Chem. Phys. Chem.*, 13 (2012) 3707.
30. V. R. Akshay, B. Arun, G. Mandal, M. Vasundhara, *Phys. Chem. Chem. Phys.*, 21 (2019) 12991.
31. Y. J. Cao, P. Wang, J. J. Fan, H. G. Yu, *Ceram. Int.*, 399 (2021) 654.
32. A. Moya, M. Barawi, B. Aleman, P. Zeller, M. Amati, A. Monreal-Bernal, L. Gregoratti, V. O'Shea, J. J. Vilatela, *Appl. Catal. B-Environ.*, 268 (2020) 118613.
33. C. J. Lin, Y. H. Liou, Y. Zhang, C. L. Chen, C. L. Dong, S. Y. Chen, G. D. Stucky, *Appl. Catal. B-Environ.*, 127 (2012) 175.
34. L. X. Deng, S. R. Wang, D. Y. Liu, B. L. Zhu, W. P. Huang, S. H. Wu, S. M. Zhang, Characterization of Fe-doped TiO₂ nanotubes with high photocatalytic activity, *Catal. Lett.*, 129 (2009) 513.
35. K. Alamelu, B. M. J. Ali, *Appl. Surf. Sci.*, 512 (2020) 145629.
36. G. Cheng, X. Liu, X. J. Song, X. Chen, W. X. Dai, R. S. Yuan, X. Z. Fu, *Appl. Catal. B-Environ.*, 277 (2020) 119196.
37. N. Özer, F. Tepehan, *Sol. Energ. Mat. Sol.*, C 56 (1999) 141.
38. J. C. Yu, J. Yu, J. Zhao, *Appl. Catal. B-Environ.*, 36 (2002) 31.
39. Z. Liu, X. Yan, W. Chu, D. Li, *Appl. Surf. Sci.*, 257 (2010) 1295.
40. M. C. Wang, H. J. Lin, T. S. Yang, *J. Alloy Compd.*, 473 (2009) 394.
41. J. Hongbo, C. Lian, *Mater. Chem. Phys.*, 77 (2002) 878.
42. S. R. Shirsath, D. V. Pinjari, P. R. Gogate, S. H. Sonawane, A. B. Pandit, *Ultrason. Sonochem.*, 20 (2013) 277.
43. M. Asiltürk, F. Sayilkan, E. Arpaç, *J. Photoch. Photobio.*, A 203 (2009) 64.
44. M. J. Valero-Romero, J. G. Santaclara, L. Oar-Arteta, L. van Koppen, D. Y. Osadchii, J. Gascon, F. Kapteijn, *Chem. Eng. J.*, 360 (2019) 75.
45. K. Elghniji, A. Atyaoui, S. Livraghi, L. Bousselmi, E. Giamello, M. Ksibi, *J. Alloy. Compd.*, 541 (2012) 421.
46. P. Kupracz, E. Coy, K. Grochowska, J. Karczewski, J. Rysz, K. Siuzdak, *Appl. Surf. Sci.*, 530 (2020) 147097.
47. Y. F. Zhu, L. Xu, J. Hu, J. Zhang, R. G. Du, C. J. Lin, *Electrochim. Acta*, 121 (2014) 361.
48. C. Feng, Z. Y. Chen, J. P. Jing, M. M. Sun, G. Y. Lu, J. Tian, J. Hou, *Corros. Sci.*, 166 (2020) 108441.
49. X.Y. Lu, L. Liu, J. W. Ge, Y. Cui, F. H. Wang, *Appl. Surf. Sci.*, 537 (2021) 148002.

50. M. T. Majd, M. Ramezanzadeh, B. Ramezanzadeh, G. Bahlakeh, *J. Hazard. Mater.*, 382 (2020) 121029.
51. A. Mahmood, G. S. Shi, Z. Wang, Z. P. Rao, W. Xiao, X. F. Xie, J. Sun, *J. Hazard. Mater.*, 401 (2021) 123402.
52. J. Yu, Q. Xiang, M. Zhou, Preparation, *Appl. Catal. B-Environ.*, 90 (2009) 595.
53. S. R. Gul, M. Khan, Z. Yi, B. Wu, *Materials*, 11 (2018) 313.

© 2021 The Authors. Published by ESG (www.electrochemsci.org). This article is an open access article distributed under the terms and conditions of the Creative Commons Attribution license (<http://creativecommons.org/licenses/by/4.0/>).